Enantiomer-Dependent Study of Photogalvanic Effects in the Multifold Fermion PdGa

Wesley E. Deeg,[1] Sujan Subedi,[1] Manita Rai,[1] Alexandre Crosbie,[1] Michael Zdilla,[2] Chandra Shekhar,[3] Claudia Felser,[3] and Darius H. Torchinsky[1,*]

[1] *Department of Physics, Temple University, Philadelphia, PA 19122*
[2] *Department of Chemistry, Temple University, Philadelphia, PA 19122*
[3] *Max Planck Institute for Chemical Physics of Solids, 01187 Dresden, Germany*

(Dated: December 3, 2025)

We report on a spectroscopic, enantiomer-dependent study of the linear (LPGE) and circular photogalvanic effect (CPGE) in the structurally chiral multifold fermion material PdGa using THz emission. Both bulk and surface responses were measured in right- and left-handed enantiomers over the $0.47 - 1.1$ eV incoming photon energy range. The effect of structural handedness was to invert the polarity of the emitted THz transients, yielding spectra roughly equal in magnitude but opposite in sign for all responses measured, with positive (negative) signals generally corresponding to right- (left-) handed samples. All spectra showed evidence of an intraband component and a previously reported interband resonance originating from transitions between the Γ and R points of the Brillouin zone. The spectra deriving from the helicoidally dispersing surface states closely matched that of the bulk, whereas the direction of the CPGE surface response rotated in opposite directions as a function of driving photon energy for the two enantiomers, revealing their complementary, helicoidally dispersing nature.

I. INTRODUCTION

Structural symmetry dictates the nature of the topological ground state [1–5]. In topological semimetals, structural symmetry protects the quasi-linearly dispersing band crossings at the Fermi energy, leading to the doubly-degenerate states of Dirac semimetals that further resolve to spin-momentum locked, nondegenerate Weyl fermions when either structural inversion symmetry or time-reversal symmetry is broken [6–8]. These band crossings are usually fixed to the same energy relative to the Fermi level E_F by mirror plane symmetries. However, the constraint on energy is relaxed in structurally chiral materials, allowing pairs of nodes to exist at time-reversal invariant points in the Brillouin zone and differ in energy by as much as hundreds of meV [9–12]. Significantly, this characteristic enables experiments that directly probe the optical consequences of topological order that derive from a single Weyl node due to Pauli blocking of its opposite chirality partner [13].

Structurally chiral crystals can be grown in two complementary structures of opposite handedness, as depicted in Figs. 1(a) and (b). The link between structure and topology implies that topological features of Weyl semimetals are inverted between right- and left-handed samples. For instance, the signs of all topological charges are flipped at the same location in $k-$space from one enantiomer to the other, as depicted in Figs. 1(c) and (d), while the spin-momentum locked Fermi arc surface states distinctive of Weyl semimetals invert the sense of their helicoidal dispersion and present Fermi surfaces whose morphologies are mirror images of one another, as shown in Figs. 1(e) and (f). Such morphological and dispersive features have been studied using angle resolved photoemission [14] and quasiparticle interference [15], however, the consequences of this dichotomy on optical response have yet to be investigated experimentally.

The nonlinear optical techniques known as the linear photogalvanic effect (LPGE) and the circular photogalvanic effect (CPGE) [16–20] are ideal platforms for demonstrating the link between structure and topology in Weyl semimetals [21–24]. These probes have recently revealed an abundance of unique phenomenology in topological semimetals, including anomalously large responses deriving from Berry curvature [25], spatially dispersive photocurrents [26], strong photocurrents of potentially topological origin deriving from linearly dispersing surface states of the bulk [27, 28], and emergent symmetry breaking in the helicoidally dispersive open Fermi arc states [29]. In a typical PGE measurement, an electromagnetic field interacts with a sample at second order to produce a DC current, either through linearly polarized fields to produce the LPGE or circularly polarized fields to generate the CPGE. The induced current is then measured through either conventional galvanometry when continuous wave sources are used, or by electro-optic sampling [30] of the THz frequency band transients emitted when the photocurrent is driven by a pulsed laser. In all cases, the measured quantity is directly proportional to the PGE response. Importantly, the sign of the measured response is preserved, in contrast with non-phase-resolved optical techniques, such as homodyne detected second harmonic generation, which report an unsigned intensity. Crucially, this allows measurements that can correlate structural symmetry and topological response.

Here, we study the interplay of structural symmetry and topological order in the structurally chiral multifold semimetal PdGa, whose helical structure is evident through the corkscrew configuration of the Ga

* dtorchin@temple.edu

atoms within the unit cell, as depicted in Figs. 1(a) and (b). PdGa belongs to the Sohncke cubic space group $P2_13$ (#198), and can be controllably grown as either enantiomer with minimal racemic twinning, providing a testbed for measurements of signed enantiomerically-derived responses. Our data, presented below, serve as such a test. Both enantiomers produce THz emission signals of equal intensity but opposite sign for LPGE and CPGE deriving from either bulk or surface. We observe an interband resonance in both responses from the surface and from the bulk at similar photon energies with comparable bandwidth. The intraband (Drude) response features prominently in the LPGE from both surface and bulk and less so in the CPGE. Finally, we note that the helicoidal dispersion of the surface states is suggested by the complementary angular dependence of the driven CPGE photocurrents for the opposite-handed materials, with the $[1\bar{1}0]$ axis serving as a mirror plane that relates the two samples. In contrast, the preferred direction of current generation in the LPGE did not vary with phonon energy, instead lying roughly along the $[1\bar{1}0]$ axis. Taken together, our results suggest PGEs as a mechanism for enantiodiscrimination in the Weyl semimetals.

II. EXPERIMENT

The laser used for this experiment produced 35 fs pulses centered at 800 nm wavelength at a 5 kHz repetition rate that seeded an optical parametric amplifier (OPA). The OPA provided a tunable $0.48-1.1$ eV excitation beam for the PGE spectrometer depicted in Fig. 2. Selection between LPGE and CPGE responses was accomplished by changing the polarization of the pump field using either a half- or quarter-wave plate, respectively. The THz transients emitted by the photocurrents were collimated by a gold-coated off-axis parabola (OAP), focused by a second OAP onto a (011) oriented ZnTe crystal and recorded by electro-optic sampling using an optical biasing technique [31, 32]. The magnitude of the measured transients thus was proportional to the photocurrent amplitude, while the photocurrent orientation was determined by resolving the horizontally and vertically polarized components of the emitted THz field.

All measurements were conducted on single crystals of PdGa that were controllably grown in either a right-or left-handed structure with respect to the positions of the Ga atoms, as illustrated in Fig. 1. Crystals were cut and polished to a mirror-finish in either the (111) orientation for bulk studies, or the (001) orientation to isolate the nonlinear responses deriving from surface states, respectively. These crystal cuts were determined to be within 1% of the stated orientation using X-ray diffractometry. For all the experiments described below, the beam propagated along the z direction of the lab frame, corresponding to the [111] direction for bulk studies or the [001] direction for surface studies.

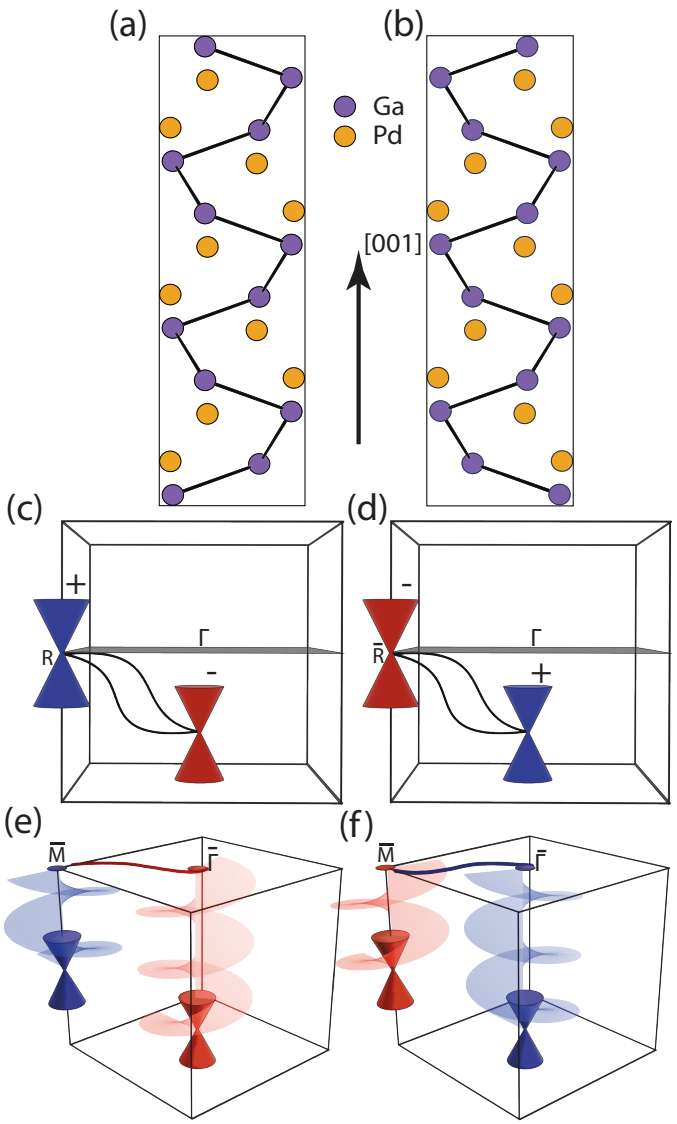

FIG. 1. Relationship between structure and topology in PdGa. (a) Left-handed and (b) right-handed enantiomer crystal structures, defined by the sense of rotation of the Ga atoms when translating through the [001] direction of the crystal. (c), (d) Depiction of the linearly dispersing Weyl cones for the left-handed (c) and right-handed (d) sample where blue and red represent opposite topological charge. The difference in energy between the nodes is due to the chiral structural symmetry. (e), (f) Depiction of the opposite helicoidally dispersing surface states and mirror image arc morphologies of the two enantiomers.

The CPGE response may be written as

$$\frac{dj_i}{dt} = \beta_{ij} \left(\mathbf{E} \times \mathbf{E}^* \right)_j \tag{1}$$

where j_i is the current in the $i = x, y, z$-direction, β_{ij} is the CPGE tensor that shares the same symmetry as the gyromagnetic tensor [24], and $\mathbf{E}$ is the electric field vector of the pump laser. Since the bulk CPGE tensor β_{ij} is proportional to the identity in $P2_13$ compounds, the bulk

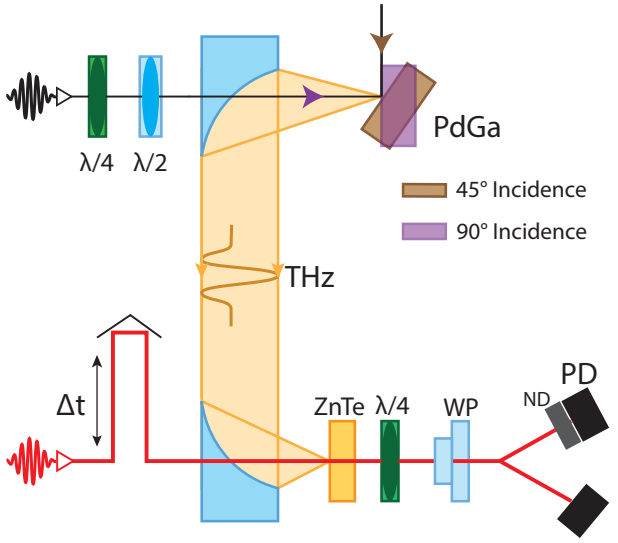

FIG. 2. Schematic of tunable THz emission spectrometer. The excitation beam was focused onto the PdGa samples at either 90° or 45° incidence. The emitted THz radiation was collimated by an off-axis parabolic (OAP) mirror and focused by a second OAP onto a ZnTe crystal for detection by electro-optic sampling (EOS) using a mechanically delayed 800 nm probe beam. After passing through the ZnTe crystal, the EOS probe beam was separated into two unbalanced components in an optical biasing configuration using a Wollaston prism and recorded by two photodiodes read out by a DAC. In our data analysis, we have taken into account the inversion of the horizontal component of the image that occurs with this configuration of OAPs.

CPGE measurements were conducted with the pump at a 45° angle of incidence with respect to the sample surface, as done in Ref. [27] and depicted in Fig. 2. This allowed for the horizontal component of the bulk photocurrent to radiate towards the OAP where it was then collected.

The LPGE is given by the expression

$$j_i = \sigma^{(2)}_{ijk} E_j E_k \tag{2}$$

where $\sigma^{(2)}_{ijk}$ is the second order conductivity that shares its symmetry with the second harmonic generation susceptibility, and E_i is the $i = x, y, z$ component of the linearly polarized electric field. The LPGE tensor in PdGa comprises only one independent element $\sigma_{xyz} = \sigma_{yzx} = \sigma_{zxy} = \sigma_{xzy} = \sigma_{zyx} = \sigma_{yxz}$ in this space group, thus the bulk LPGE response was measured at normal incidence in (111) oriented samples by separately recording the horizontally (H) and vertically (V) polarized THz transients as a function of the incoming pump polarization ϕ to resolve the components of j_i.

Surface measurements of CPGE and LPGE were conducted at normal incidence on (001) oriented PdGa in a manner described in the literature [29, 33]. Briefly, the (001) surface of P2$_1$3 crystals lacks structural surface symmetry due to the nonsymmorphic screw axis along [001]. The consequence is an unconstrained surface CPGE tensor β_{ij} that comprises several independent off-diagonal elements, e.g., β_{xz}, which produce photocurrents transverse to a normally incident driving field aligned with the z-axis, while the bulk photocurrents are longitudinal to the excitation. The LPGE tensor is similarly unconstrained and, through elements such as, e.g., σ_{xxy}, also produce transverse surface currents. As a consequence of these transverse surface photocurrents and longitudinal bulk photocurrents, the radiation from the former can be collected by the OAPs and measured while that from the latter does not reach the OAPs. In our experiments, we indexed the [100] axis using an X-ray diffractometer and aligned it by eye with the lab frame x-axis. Both horizontal and vertical polarizations of the emitted THz were measured for the CPGE and LPGE responses as a function of photon energy. In the case of the LPGE, spectra were also acquired as a function incoming photon polarization angle ϕ.

In order to correlate the spectral measurements with the structural symmetry, we also measured the positions of the Ga atoms as a function of position for both enantiomers using X-ray diffractometry. Single-crystal X-ray diffraction was performed on a Bruker Kappa PHOTON III DUO diffractometer equipped with an Oxford Cryostream 700 variable temperature system. Data were collected at 100 K. The collection strategy was determined using the Bruker Suite. Integration was performed using SAINT and data were scaled using SADABS. The determination of the space group was made using XPREP, while the structure was solved using intrinsic phasing with the program SHELXT [34] and refined using the SHELX suite [35] using Olex2 v. 1-5 as a GUI [36]. Following structure solution and refinement, the absolute structure was determined by refinement of the Flack parameter [37], which was measured as 0.010 ± 0.04 for the left-handed sample and -0.001 ± 0.032 for the right-handed sample indicating high degrees of enantiomeric purity. Below, we denote the sample with Ga atoms arranged clockwise as the sample is translated positively in [001] as being left-handed (as in Fig. 1(a)) and those arrange counterclockwise as right-handed (as in Fig. 1(b)).

We note that PdGa is not ideal for studying the relationship between topological order and structural chirality because, as noted below, its Fermi level is offset from the multifold points, thereby suppressing optical and electronic responses of topological origin. Thus, the complementary nature of the bulk photocurrents discussed in the text should be viewed as more representative of structural effects than topological ones. However, $P2_13$ materials whose Fermi levels are more favorable to investigate bulk-derived topological effects, such as RhSi and CoSi, cannot be selectively grown as either enantiomer at this time, making PdGa the best choice for this study.

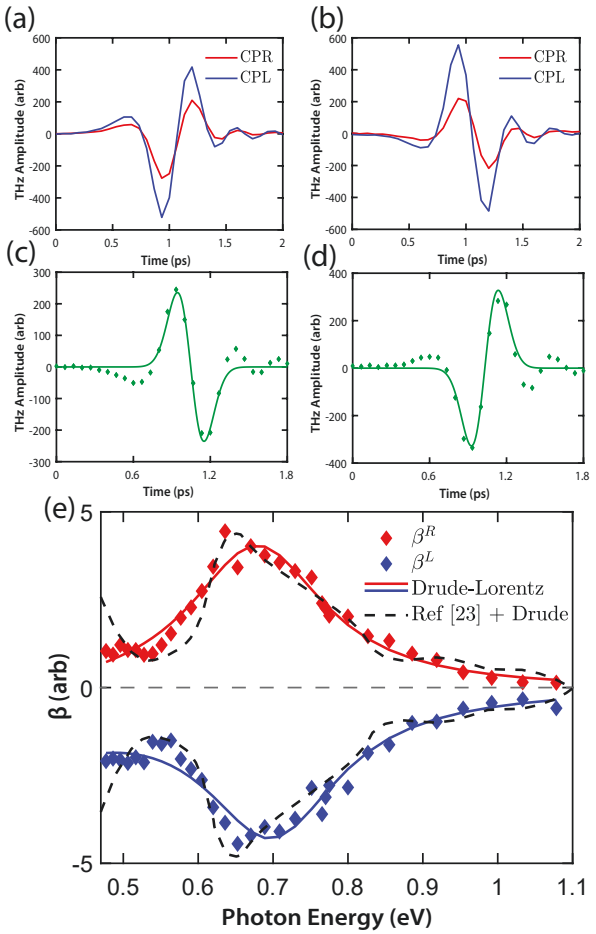

FIG. 3. Representative CPGE THz transients and bulk CPGE spectrum with results for the left-handed sample in the left panels and the right-handed sample in the right panel. (a), (b) THz emission transients for circularly polarized right (CPR) and left (CPL) excitation in PdGa at 0.69 eV incident photon energy and 45° angle of incidence. (c), (d) CPGE transients obtained by subtraction of CPR by CPL. Also shown is a fit to the model function described in the text. (e) CPGE spectrum for both enantiomers. Fits to the Drude-Lorentz model are shown in solid lines and fits to the calculation in Ref. [23] added to an intraband component are shown in dashed lines.

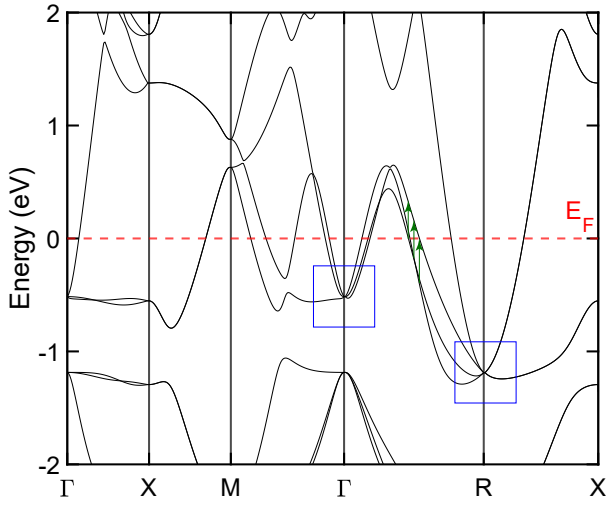

FIG. 4. Low energy band structure of PdGa. The Fermi level is denoted by the dashed red line, the multifold points are enclosed in blue boxes, and representative interband transitions relating to the resonance seen in Fig. 3(e) are depicted by the green arrows in between the high symmetry points at Γ and R.

III. RESULTS AND DISCUSSION

A. Bulk CPGE Response

Representative THz transients of the bulk CPGE are shown in Figs. 3(a) and (b) for the left and right-handed samples, respectively. Only the horizontal (H) component of the photocurrent is shown as the vertical component deriving from the surface was too weak to be accurately measured, in agreement with the bulk point group symmetry. We observed a brief, ∼ 1 ps THz frequency band transient that changed in magnitude but did not fully invert as the helicity of the driving radiation was switched, indicating contributions from non-CPGE sources. In order to isolate the CPGE response, we subtracted the transients measured with the left-circularly polarized pump from those driven by a right-circularly polarized pump, as shown in Figs. 3(c) and (d). The differenced data were fitted to the first derivative of a Gaussian function (shown), which provided a good empirical description of the response.

The amplitude parameter of this fit obtained as a function of pump photon energy was used as a measure of the CPGE magnitude after normalization by the wavelength-dependent laser power and spot size. The result is plotted in Fig. 3(e). Both spectra are of equal magnitude but opposite in sign with the right-handed sample producing a positively signed response and the left-handed sample producing a negative one. Notably, we observe that the CPGE amplitude is small but non-zero at low energy, and then peaks at ∼ 0.7 eV before receding again to a lower value at greater photon energy. This peak is in good agreement with experimental measurements of the linear optical conductivity in PdGa [38]. Specifically, DFT calculations assign this feature to interband transitions between quasiparallel bands midway between the Γ and R points of the Brillouin zone [38, 39].

A band structure for PdGa taken from the Materials Project [40] is shown in Fig. 4 to facilitate interpretation of the data. As can be seen in the Figure, the Fermi level is higher than the multifold points at Γ and R by ∼ 0.5 eV and ∼ 1 eV, respectively [38], making this material more akin to a metal than a semimetal, suggesting the nonzero low-frequency response is due to conduction electrons. Thus, we may empirically describe the data by Drude-Lorentz fits, shown as solid lines in Fig. 3(e), where the Drude component captures the offset and the

Lorentz component accounts for the resonance. Using the single Drude linewidth of ~ 0.089 eV from Ref. [38], we obtained 0.70 ± 0.01 eV as the single resonance energy with a linewidth of 0.23 ± 0.03 eV for the right-handed sample, and 0.69 ± 0.01 eV with a linewidth of 0.22 ± 0.03 eV for the left-handed sample.

We may also compare the data of Fig. 3(e) with theoretical predictions for the interband contribution to the CPGE in PdGa as calculated by Le and Sun [23]. The prediction is shown in the panel after rescaling to match the arbitrary amplitude of the data. We have separately added a Drude component to account for the conduction electron response. There is good agreement between theory and experiment over the energy range studied.

B. Bulk LPGE Response

We now turn to LPGE measurements, which were conducted at normal incidence to (111) as a function of both polarization angle of the incident beam ϕ and photon energy. Example THz transients are shown in Figs 5(a) and (b). The data were determined to be best empirically described by the second derivative of a Gaussian function, as shown in the Figures. The amplitude parameter from the fits was used to produce plots of the rotational anisotropy (i.e., the ϕ dependence) of both the H and V emitted THz polarizations as shown in Fig. 5(c) and (d). We have denoted the positive and negative phase signals on the polar plot by $+$ and $-$, respectively. Comparing the two enantiomers, we note that the rotational anisotropy plots are identical yet complementary in sign.

Since the projection of the [100] axis onto the (111) plane was aligned with the lab-frame x-axis as shown in the Figure, the data are theoretically described by

$$j_x = -\sigma_{xyz} \cos(2\phi + \psi) \quad (3)$$

$$j_y = -\sigma_{xyz} \sin(2\phi + \psi)\,. \quad (4)$$

Fits yielded values of $\psi = 14.8°$, in agreement with the bulk point group symmetry and crystal orientation. After normalizing by laser power and spot size, we thus obtained a spectrum proportional to the conductivity $\sigma^{(2)}_{xyz}$ as a function of incoming photon energy.

The LPGE spectra are plotted in Fig. 5(e). As with the CPGE data, the two spectra are of approximately equal magnitude but opposite sign across the range of photon energies measured, with the right-handed enantiomer producing a positively signed spectrum and the left-handed enantiomer yielding a negatively signed spectrum. In both plots, there is a peak in the data at ~ 0.75 eV. Notably, the data are markedly stronger at lower photon energy for both samples, with the measured intensity appearing to increase as the photon energy is reduced. This observation is consistent with the source of LPGE shifting from interband transitions roughly centered at 0.75 eV to a Drude source derived from the conduction electrons at lower energy. This Drude response

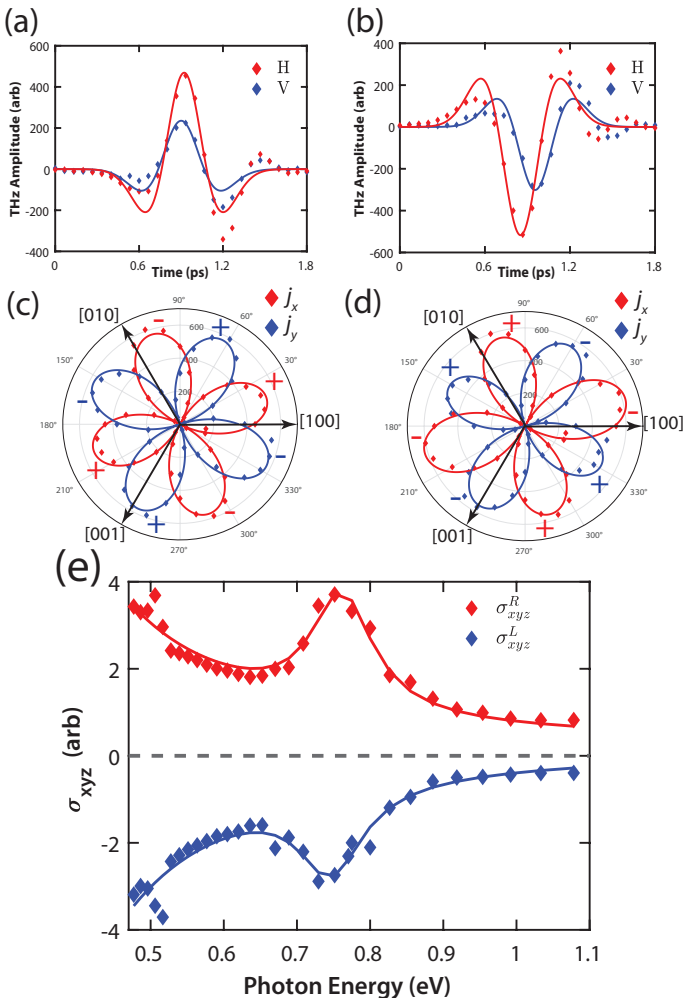

FIG. 5. Representative LPGE THz transients and bulk LPGE spectrum with results for the left-handed sample on the left and the right-handed sample on the right. (a), (b) Representative LPGE THz transients for the same polarization of the pump beam relative to the projection of the [100] axis. The data for both horizontally and vertically polarized emitted THz transients are shown as dots while the fits to the model function described in the text are shown as solid lines. (c), (d) LPGE rotational anisotropy traces for the horizontally and vertically-resolved current components as a function of incoming polarization angle. The solid line is a fit to the model function described in the text, with positive phase signals shown with a $+$ next to them and negative signals with a $-$ next to them. (e) LPGE spectra for both the left and right-handed samples with data shown as points and the Drude-Lorentz fits as lines. The resonance feature at ~ 0.7 eV likely shares the same origin as the resonance feature observed in bulk CPGE.

dominates the linear optical conductivity up to an energy scale of ≈ 0.5 eV [38], which is within our measurement window.

Following our analysis of the CPGE spectra, we fit the LPGE spectra with a Drude-Lorentz function using the Drude parameters of Ref. [38]. We determined

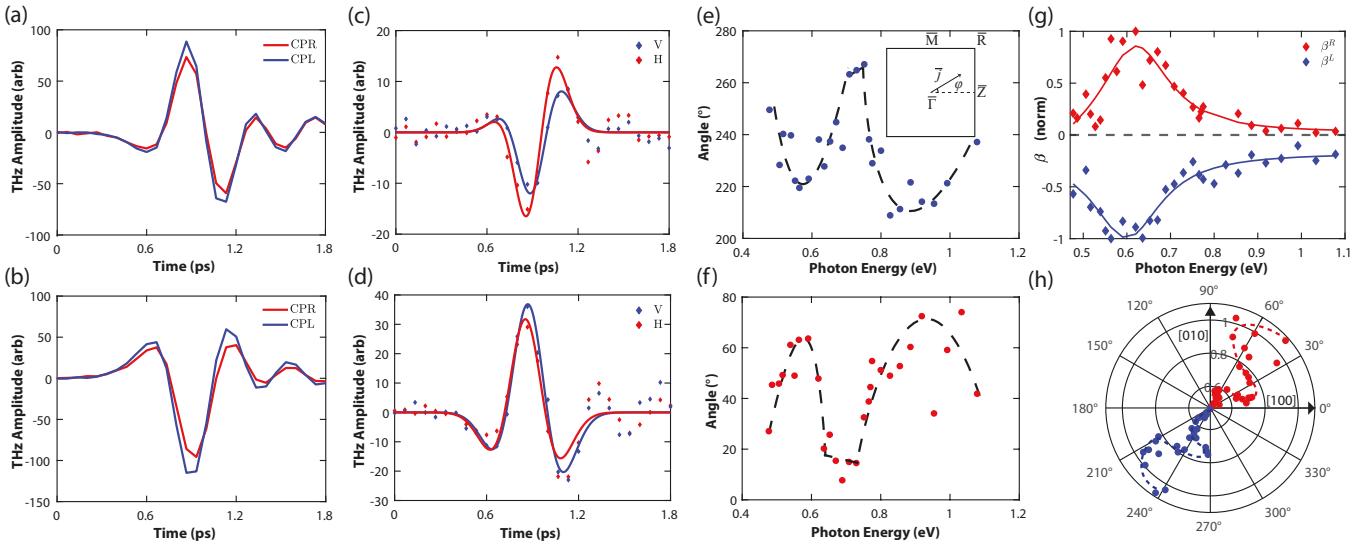

FIG. 6. Representative CPGE THz transients and surface CPGE spectrum. (a), (b) THz emission transients for circularly polarized right (CPR) and left (CPL) excitation in the PdGa (001) oriented samples at 0.65 eV incident photon energy and 0° angle of incidence. (c), (d) Representative CPGE transients obtained by subtraction of CPR and CPL at 0.65 eV pump energy. Also shown is a fit to the model function discussed in the text. (e), (f) Calculated angular dependence of the CPGE current for the (001) oriented right-handed sample along with lines to guide the eye. The inset to panel (e) shows the definition of the plotted angle ϕ relative to the surface Brilloiun zone. (g) Amplitudes of the individual fits of CPGE data as a function of incident photon energy for the right-handed sample (red) and the left-handed sample (blue). (h) Polar coordinate representation of (001) surface CPGE angular dependence on energy, with [100] axis corresponding to 0° and the [010] axis corresponding to 90°.

that the resonance energy was at 0.74 ± 0.01 eV with a linewidth of 0.08 ± 0.02 eV for the right-handed sample, and 0.76 ± 0.01 eV with a linewidth of 0.12 ± 0.04 eV for the left-handed sample. In this case, the resonances were both slightly higher in energy and of considerably narrower linewidth than was observed in CPGE. It is not unexpected to see slightly different spectral features for the two responses; the LPGE and CPGE obey separate optical selection rules and thus may sample interband transitions differently.

C. Surface CPGE Response

We next turn to the helicoidally dispersing Fermi arc surface states by applying the PGE technique to PdGa in a similar manner as previous done on isostructural RhSi [29]. The surface CPGE response was measured over the $0.47 - 1.1$ eV photon energy range and the THz radiation emitted from the sample resolved into H and V components. Even though the bulk symmetry of the crystal is cubic, meaning that [100] is equivalent to [010], the nonsymmorphic space group results in a lack of surface symmetry. We thus chose [100] and [010] so that the crystal axes described a right-handed coordinate system in the lab frame. Following Ref. [29], we also verified that the response derived exclusively from the surface by rotating the sample through an angle $\phi \in [0, 2\pi]$, and observed that the amplitude of the horizontal component of the CPGE varied as $\sim \cos(\phi)$ and that of the vertical component varied as $\sim \sin(\phi)$, as expected.

Raw data traces in Fig. 6(a) and (b) show the individual transients measured under excitation from right and left circularly polarized light for the right-handed and left-handed samples, respectively. While the individual transients are measurable with good signal to noise, the CPGE signal that derives from their difference is much weaker in comparison with the bulk, i.e., by a factor of ~ 15 for both samples. A representative data trace of the isolated CPGE response is shown in Figs. 6(c) and (d), which is fit to the linear combination of the first and second derivatives of a Gaussian function to phenomenologically analyze the response. The coefficient of the first derivative of a Gaussian was then used to determine the CPGE tensor parameters, i.e., the magnitude of the H-polarized component was identified as the surface CPGE tensor element β_{xz}, while that of the V-component identified as β_{yz}. This allowed us to compute the direction of the CPGE transient as $\tan^{-1}(\beta_{yz}/\beta_{xz})$ for the two samples, as shown in Figs. 6(e) and (f). The spectral amplitude was given by $\pm\sqrt{\beta_{xz}^2 + \beta_{yz}^2}$ and is plotted as a spectrum in Fig. 6(g) with the sign determined by the quadrant in which the CPGE current vector lies. We will first discuss the spectral amplitude and then the energy dependence of the CPGE direction.

As with the bulk data, the magnitude spectra in Fig. 6(g) are approximately equal in amplitude but opposite in sign; the spectrum is positive for the right-

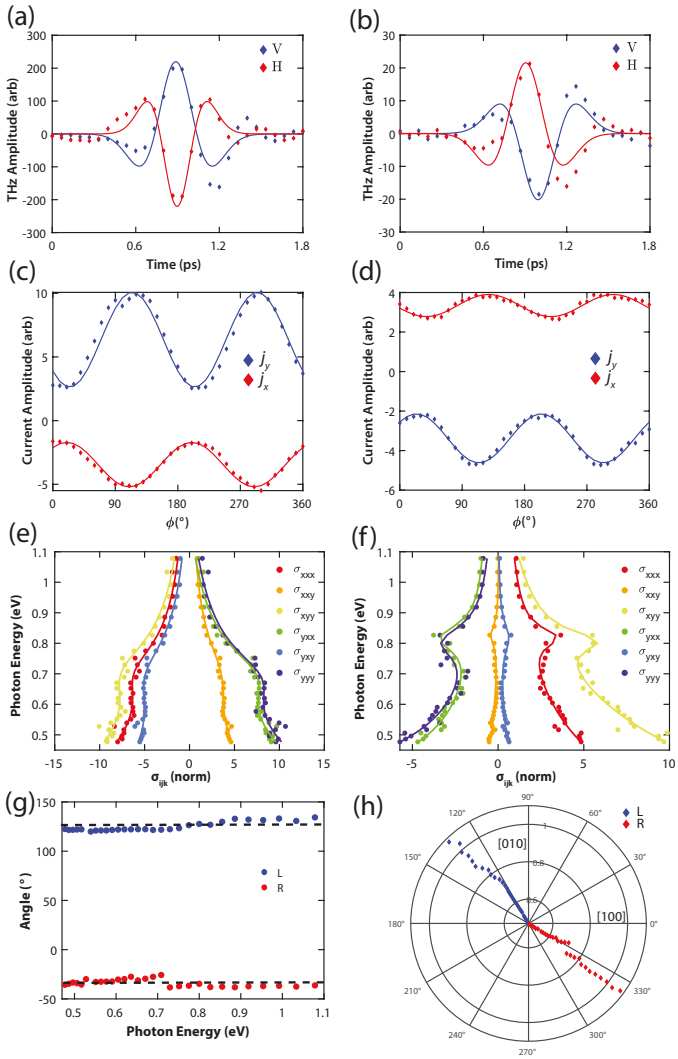

FIG. 7. Representative surface LPGE THz transients and spectrum. (a), (b) Representative LPGE THz transients with a pump beam polarized at 10° relative to the lab-frame x-axis. The data for both horizontally and vertically polarized emitted THz transients are shown as dots while the fits to the model function described in the text are shown as solid lines. (c), (d) LPGE rotational anisotropy traces for the horizontally and vertically-resolved current components as a function of incoming polarization angle across a range of energies. The solid line is a fit to the model function described in the text. (e), (f) Individual LPGE tensor elements σ_{ijk} for both the left and right-handed samples, fitted to Drude-Lorentz functions. (g) Plot of preferred "direction" of surface LPGE plotted as a function of photon energy which is shown in panel (h) to approximately lie along the $[1\bar{1}0]$ axis about which the CPGE response is reflected for the two samples.

handed sample and negative for the left-handed one. There is a peak in the spectrum at a lower photon energy as compared with the bulk value of ~ 0.7 eV. This observation is consistent with previous measurements of surface CPGE in RhSi that also yielded similar spectra for the surface and bulk CPGE responses [27, 29]. We modeled the data using a Drude-Lorentz function, obtaining a resonance energy of 0.58 ± 0.01 eV with a linewidth of 0.18 ± 0.10 eV for the left-handed enantiomer, and a resonance energy of 0.62 ± 0.01 eV with a linewidth of 0.23 ± 0.09 eV for the right-handed enantiomer.

Owing to the lack of surface symmetry, the angle subtended by the CPGE current relative to the [100] axis is unconstrained. CPGE transients that derive from optical interband transitions produce photocurrents oriented in the direction given by the location in k-space where these transitions occur in the dispersing helicoid. In the case of the bulk of Weyl semimetals, the orientation of the current is not expected to change with photon energy, since the linear dispersion of the Weyl cone ensures that the transitions occur in the same direction in k but with changing magnitude. In the case of helicoidal dispersion, as is relevant here, the points connected by the vertical transition may vary in k_x and k_y as different points of the helicoid are connected by the change in photon energy, hence allowing the direction of the emitted photocurrent to vary. Since the helicoids of the two opposite enantiomers disperse with opposite helicity, we expect the angular variation to be mirror images of one another when reflected about an axis on the surface.

These expectations are borne out by the data presented in Fig. 6(e) and (f), where we plot the angle of the photocurrent relative to the [100] axis as a function of incoming photon energy. We observe complementary behavior for the two enantiomers as the angular variation for both is on the order of 60°. When these data are plotted together on the polar axes of Fig. 6(h), we note that the angular variation in the direction of the CPGE of the two enantiomers is approximately reflected about the $[1\bar{1}0]$ axis to within our ability to resolve it in our experimental setup.

D. Surface LPGE Response

Finally, measurements of LPGE responses from the (001) surface were taken at normal incidence. The raw data for the individual transients are shown in Figs. 7(a) and (b). Each individual transient was fit to the second derivative of a Gaussian, from which we obtained an amplitude parameter that was used to construct rotational anisotropy plots, an example of which is shown in Figs. 7(c) and (d). As with the previous measurements, the relationship between the two data sets shows that switching from one enantiomer to the other inverts the overall sign of the signal.

The photocurrent response for a normally incident beam propagating along the laboratory z-axis is described as

$$j_i = \sigma^{(2)}_{ixx} \cos^2(\phi) + 2\sigma^{(2)}_{ixy} \cos(\phi) \sin(\phi) + \sigma^{(2)}_{iyy} \sin^2(\phi) \quad (5)$$

where j_i is the photocurrent in the $i = x, y$ direction. Following Ref. [29], the data were more accurately described

by fitting both the horizontally and vertically polarized THz emission transients to the expression

$$j_i = A_i \cos(\phi - \psi_i) + B_i, \tag{6}$$

and using the relationships

$$\sigma_{ixx} = B_i + A_i \cos(\psi_i) \tag{7}$$
$$\sigma_{ixy} = A_i \sin(\psi_i) \tag{8}$$
$$\sigma_{iyy} = B_i - A_i \cos(\psi_i) \tag{9}$$

to recover the individual tensor elements σ_{ijk}.

Figures 7(e) and (f) show plots of these individual tensor elements normalized to the value of σ_{yxx} at 1.1 eV. We again note the approximate mirror image relationship between them. As can be seen in the data, the interband resonance clearly observed in the other responses was only weakly perceptible in any of the individual tensor elements while the intraband response was dominant. This may indicate that conduction electrons play a much larger role relative to interband transitions in yielding surface LPGE responses than they do in the bulk. We modeled each element using a Drude-Lorentz response individually and provide the full list of all the relevant fitting parameters in Table I. We obtained an average Drude width of 0.71 ± 0.14 eV for the left-handed sample and 0.51 ± 0.14 eV for the right-handed sample. Similarly, the resonance energy of the left-handed sample was, on average, at 0.71 ± 0.01 eV with an average linewidth of 0.24 ± 0.12 eV, while the averaged right-handed sample parameters were 0.82 ± 0.01 eV for the resonance energy and 0.10 ± 0.03 eV for the linewidth. We note that there is a ~ 100 meV difference in the measured interband resonance energy between the two enantiomers. We speculate that such a large discrepancy between the fitted values of the Lorentzian resonance energy may be partially due to differences in residual strain from polishing the surfaces, however further investigation is required to fully account for the shift.

It is not possible to construct a vector from the LPGE response since it comprises six independent tensor elements. We thus defined a preferred "direction" of THz emission by computing an angle as $\tan^{-1}(B_y/B_x)$. In other words, the offsets of the fitted trigonometric functions for both H- and V- polarized emitted THz transients were used as proxies for the ϕ-averaged amount of current in the x and y directions at each phonon energy. The results are plotted in Fig. 7(g) and (h), where we see that the angle is fixed at $\sim -35°$ for the right-handed sample and 120° for the left-handed one, i.e., approximately along the axis of reflection between the two enantiomers for the angular CPGE data of Fig. 6(h).

Considering the CPGE and LPGE data of Figs. 6 and 7, respectively, in the context of the previous photogalvanic study of RhSi [29] highlights an important difference between the two isostructural multifold fermion materials. In RhSi, the CPGE response was largely pinned to the [100] axis (specifically, $\frac{dj_y}{dt} \approx 0$) over the $0.7 - 1.2$ eV incoming photon energy range, which coincided with the interval over which its LPGE tensor parameters obeyed the approximate relationships $\sigma_{xxx} \approx \sigma_{xyy} \approx \sigma_{yxy} \approx \sigma_{yyy}$ and $\sigma_{xxy} \approx \sigma_{yxx} \approx 0$. Taken together, these approximate equalities were consistent with [100] serving as an emergent mirror axis, the qualification on symmetry arising from the limited incoming photon energy interval of the observation. No such relationships between LPGE tensor elements are observed in PdGa, while the CPGE current vector subtends a larger range of angles over the same range of pump energies, indicating no such emergent symmetry. This suggests that further research on the nature of RhSi surface states is warranted, particularly in light of evidence that isostructural CoSi hosts a charge density wave instability [41–43].

More broadly, our results suggest that enantiodiscrimination is feasible without knowing the handedness of the crystal a priori. CPGE responses were uniformly positive for the bulk and surface responses of the right-handed sample and negative in either case for the left-handed one. In the event that topological sources dominate this response, as suggested by Ref. [27], it may be possible to determine the sign of the topological charge directly using this technique. Similarly, the bulk LPGE tensor element σ_{xyz} was positive for the right-handed sample and negative for its left-handed counterpart, suggesting that, in addition to the CPGE, the LPGE could also be used to determine the handedness of the crystal and thereby the sign of its topological charge.

IV. CONCLUSIONS

We have demonstrated the interplay of structural chirality and nonlinear optical response in Weyl semimetals using THz emission photogalvanic effect spectroscopy in the multifold semimetal PdGa. LPGE and CPGE spectra of the bulk were of approximately the same magnitude but opposite sign, with right-handed samples producing positively signed signals and left-handed samples negatively signed ones, suggesting a route toward enantiodiscrimination in Weyl semimetals. All obtained spectra were well described by Drude-Lorentz fits that were in good agreement with linear optical spectroscopy, while the bulk CPGE data were well described by theory [23] when a separate intraband component was included. Direct observation of surface state CPGE and LPGE revealed that the amplitude spectra were similar in peak energy and width to the bulk spectra that were also adequately modeled by a Drude-Lorentz model. The presence of the helicoidally dispersing surface states was evident in the CPGE response through the evolution of the photocurrent direction as a function of driving photon energy, which was mirrored across bulk [110] crystalline axes for the two enantiomers. However, we observed no emergent symmetry in the PGE response of the PdGa surface states, in contrast with previous measurements on isostructural RhSi.

	Left			Right		
	γ_D	E_0	γ_0	γ_D	E_0	γ_0
σ_{xxx}	0.61 ± 0.09	0.71 ± 0.01	0.23 ± 0.10	0.6 ± 0.2	0.82 ± 0.01	0.08 ± 0.02
σ_{xxy}	0.65 ± 0.11	0.71 ± 0.01	0.27 ± 0.13	0.5 ± 0.2	0.83 ± 0.01	0.07 ± 0.02
σ_{xyy}	0.76 ± 0.15	0.72 ± 0.01	0.25 ± 0.13	0.74 ± 0.09	0.81 ± 0.01	0.08 ± 0.02
σ_{yxx}	0.73 ± 0.11	0.70 ± 0.01	0.23 ± 0.10	0.41 ± 0.08	0.82 ± 0.01	0.11 ± 0.02
σ_{yxy}	0.8 ± 0.2	0.71 ± 0.01	0.23 ± 0.13	0.4 ± 0.2	0.82 ± 0.01	0.12 ± 0.03
σ_{yyy}	0.72 ± 0.14	0.70 ± 0.01	0.23 ± 0.13	0.41 ± 0.08	0.81 ± 0.01	0.12 ± 0.04
Mean	0.71 ± 0.13	0.71 ± 0.01	0.24 ± 0.12	0.51 ± 0.14	0.82 ± 0.01	0.10 ± 0.03

TABLE I. Table of fitted Drude-Lorentz values and their uncertainties for the surface LPGE conductivities σ_{ijk} plotted in Figs. 7(e) and (f). γ_D is the fitted Drude width, E_0 is the resonance energy and γ_0 is the resonance linewidth. All quantities are in units of eV.

V. ACKNOWLEDGMENTS

We acknowledge funding by the National Science Foundation under Grant No. NSF/DMR-1945222. NSF MRI grant CHE-2215854 is acknowledged for the X-ray crystallographic studies. We also acknowledge support from the Deutsche Forschungsgemeinschaft (DFG) under SFB1143 (Project No. 247310070), the Würzburg-Dresden Cluster of Excellence on Complexity and Topology in Quantum Matter—ct.qmat (EXC 2147, Project No. 390858490) and the QUAST-FOR5249-449872909.

DATA AVAILABILITY

The raw data supporting the findings of this study are openly available [44].

[1] M. Z. Hasan and C. L. Kane, Colloquium: Topological insulators, Rev. Mod. Phys. **82**, 3045 (2010).
[2] N. P. Armitage, E. J. Mele, and A. Vishwanath, Weyl and dirac semimetals in three-dimensional solids, Rev. Mod. Phys. **90**, 015001 (2018).
[3] B. J. Wieder, B. Bradlyn, J. Cano, Z. Wang, M. G. Vergniory, L. Elcoro, A. A. Soluyanov, C. Felser, T. Neupert, N. Regnault, and B. A. Bernevig, Topological materials discovery from crystal symmetry, Nature Reviews Materials **7**, 196 (2022).
[4] H. Gao, J. W. Venderbos, Y. Kim, and A. M. Rappe, Topological semimetals from first principles, Annual Review of Materials Research **49**, 153 (2019).
[5] T. Senthil, Symmetry-protected topological phases of quantum matter, Annu. Rev. Condens. Matter Phys. **6**, 299 (2015).
[6] C. Fang, L. Lu, J. Liu, , and L. Fu, Topological semimetals with helicoid surface states, Nature Physics **12** (1982).
[7] S. Jia, S.-Y. Xu, , and M. Z. Hasan, Weyl semimetals, fermi arcs and chiral anomalies (a short review), Nature Mater **15**, 1140 (2016).
[8] M. Z. Hasan, G. Chang, I. Belopolski, G. Bian, S.-Y. Xu, and J.-X. Yin, Weyl, Dirac and high-fold chiral fermions in topological quantum matter, Nature Review Mater **6** (2021).
[9] G. Chang, B. J. Wieder, F. Schindler, D. S. Sanchez, I. Belopolski, S.-M. Huang, B. Singh, D. Wu, T.-R. Chang, T. Neupert, S.-Y. Xu, H. Lin, and M. Z. Hasan, Topological quantum properties of chiral crystals, Nature materials **17**, 978 (2018).
[10] N. B. Schröter, D. Pei, M. G. Vergniory, Y. Sun, K. Manna, F. De Juan, J. A. Krieger, V. Süss, M. Schmidt, P. Dudin, B. Bradlyn, T. K. Kim, T. Schmitt, C. Cacho, C. Felser, V. N. Strocov, and Y. Chen, Chiral topological semimetal with multifold band crossings and long fermi arcs, Nature Physics **15**, 759 (2019).
[11] D. S. Sanchez, I. Belopolski, T. A. Cochran, X. Xu, J.-X. Yin, G. Chang, W. Xie, K. Manna, V. Süß, C.-Y. Huang, N. Alidoust, D. Multer, S. S. Zhang, N. Shumiya, X. Wang, G.-Q. Wang, T.-R. Chang, C. Felser, S.-Y. Xu, S. Jia, H. Lin, and M. Z. Hasan, Topological chiral crystals with helicoid-arc quantum states, Nature **567**, 500 (2019).
[12] Z. Rao, H. Li, T. Zhang, S. Tian, C. Li, B. Fu, C. Tang, L. Wang, Z. Li, W. Fan, J. Li, Y. Huang, Z. Liu, Y. Long, C. Fang, H. Weng, Y. Shi, H. Lei, Y. Sun, Q. Tian, and H. Ding, Observation of unconventional chiral fermions with long fermi arcs in cosi, Nature **567**, 496 (2019).
[13] F. De Juan, A. G. Grushin, T. Morimoto, and J. E. Moore, Quantized circular photogalvanic effect in Weyl semimetals, Nature communications **8**, 15995 (2017).
[14] Y. Yen, J. A. Krieger, M. Yao, I. Robredo, K. Manna, Q. Yang, E. C. McFarlane, C. Shekhar, H. Borrmann, S. Stolz, R. Widmer, O. Gröning, V. N. Strocov, S. S. P. Parkin, C. Felser, M. G. Vergniory, M. Schüler, and N. B. M. Schröter, Controllable orbital angular momentum monopoles in chiral topological semimetals, Nature Physics , 1 (2024).
[15] P. Sessi, F.-R. Fan, F. Küster, K. Manna, N. B. M. Schröter, J.-R. Ji, S. Stolz, J. A. Krieger, D. Pei, T. K. Kim, P. Dudin, C. Cacho, R. Widmer, H. Borrmann, W. Shi, K. Chang, Y. Sun, C. Felser, and S. S. P. Parkin, Handedness-dependent quasiparticle interference

in the two enantiomers of the topological chiral semimetal PdGa, Nature Communications **11**, 3507 (2020).
[16] V. I. Belinicher and B. I. Sturman, The photogalvanic effect in media lacking a center of symmetry, Soviet Physics Uspekhi **23**, 199 (1980).
[17] J. Sipe and A. Shkrebtii, Second-order optical response in semiconductors, Physical Review B **61**, 5337 (2000).
[18] E. L. Ivchenko, *Optical spectroscopy of semiconductor nanostructures* (Alpha Science Int'l Ltd., 2005).
[19] S. Ganichev, E. Ivchenko, and W. Prettl, Photogalvanic effects in quantum wells, Physica E: Low-dimensional Systems and Nanostructures **14**, 166 (2002).
[20] S. D. Ganichev and L. E. Golub, Interplay of rashba/dresselhaus spin splittings probed by photogalvanic spectroscopy–a review, physica status solidi (b) **251**, 1801 (2014).
[21] Y. Zhang, H. Ishizuka, J. van den Brink, C. Felser, B. Yan, and N. Nagaosa, Photogalvanic effect in weyl semimetals from first principles, Physical Review B **97**, 241118 (2018).
[22] Y. Sun, Q. Xu, Y. Zhang, C. Le, and C. Felser, Optical method to detect the relationship between chirality of reciprocal space chiral multifold fermions and real space chiral crystals, Phys. Rev. B **102**, 104111 (2020).
[23] C. Le and Y. Sun, Topology and symmetry of circular photogalvanic effect in the chiral multifold semimetals: a review, Journal of Physics: Condensed Matter **33**, 503003 (2021).
[24] J. Orenstein, J. Moore, T. Morimoto, D. Torchinsky, J. Harter, and D. Hsieh, Topology and symmetry of quantum materials via nonlinear optical responses, Annual Review of Condensed Matter Physics **12**, 247 (2021).
[25] G. B. Osterhoudt, L. K. Diebel, M. J. Gray, X. Yang, J. Stanco, X. Huang, B. Shen, N. Ni, P. J. Moll, Y. Ran, and K. S. Burch, Colossal mid-infrared bulk photovoltaic effect in a type-I Weyl semimetal, Nature Materials **18**, 471 (2019).
[26] Z. Ji, G. Liu, Z. Addison, W. Liu, P. Yu, H. Gao, Z. Liu, A. M. Rappe, C. L. Kane, E. J. Mele, and R. Agarwal, Spatially dispersive circular photogalvanic effect in a weyl semimetal, Nature materials **18**, 955 (2019).
[27] D. Rees, K. Manna, B. Lu, T. Morimoto, H. Borrmann, C. Felser, J. Moore, D. H. Torchinsky, and J. Orenstein, Helicity-dependent photocurrents in the chiral Weyl semimetal RhSi, Science advances **6**, eaba0509 (2020).
[28] Z. Ni, K. Wang, Y. Zhang, O. Pozo, B. Xu, X. Han, K. Manna, J. Paglione, C. Felser, A. G. Grushin, F. de Juan, E. Mele, and L. Wu, Giant topological longitudinal circular photo-galvanic effect in the chiral multifold semimetal CoSi, Nature communications **12**, 154 (2021).
[29] D. Rees, B. Lu, Y. Sun, K. Manna, R. Özgür, S. Subedi, H. Borrmann, C. Felser, J. Orenstein, and D. H. Torchinsky, Direct measurement of helicoid surface states in RhSi using nonlinear optics, Phys. Rev. Lett. **127**, 157405 (2021).
[30] Q. Wu and X.-C. Zhang, Free-space electro-optic sampling of terahertz beams, Applied Physics Letters **67**, 3523 (1995).
[31] F. D. J. Brunner, J. A. Johnson, S. Grübel, A. Ferrer, S. L. Johnson, and T. Feurer, Distortion-free enhancement of terahertz signals measured by electro-optic sampling. i. theory, J. Opt. Soc. Am. B **31**, 904 (2014).
[32] J. A. Johnson, F. D. J. Brunner, S. Grübel, A. Ferrer, S. L. Johnson, and T. Feurer, Distortion-free enhancement of terahertz signals measured by electro-optic sampling. ii. experiment, J. Opt. Soc. Am. B **31**, 1035 (2014).
[33] G. Chang, J.-X. Yin, T. Neupert, D. S. Sanchez, I. Belopolski, S. S. Zhang, T. A. Cochran, Z. Chéng, M.-C. Hsu, S.-M. Huang, B. Lian, S.-Y. Xu, H. Lin, and M. Z. Hasan, Unconventional photocurrents from surface Fermi arcs in topological chiral semimetals, Phys. Rev. Lett. **124**, 166404 (2020).
[34] G. M. Sheldrick, Shelxt–integrated space-group and crystal-structure determination, Acta Crystallographica Section A: Foundations and Advances **71**, 3 (2015).
[35] G. M. Sheldrick, Crystal structure refinement with shelxl, Acta Crystallographica Section C: Structural Chemistry **71**, 3 (2015).
[36] O. V. Dolomanov, L. J. Bourhis, R. J. Gildea, J. A. Howard, and H. Puschmann, Olex2: a complete structure solution, refinement and analysis program, Journal of applied crystallography **42**, 339 (2009).
[37] H. Flack, On enantiomorph-polarity estimation, Acta Crystallographica Section A: Foundations of Crystallography **39**, 876 (1983).
[38] L. Maulana, Z. Li, E. Uykur, K. Manna, S. Polatkan, C. Felser, M. Dressel, and A. Pronin, Broadband optical conductivity of the chiral multifold semimetal PdGa, Physical Review B **103**, 115206 (2021).
[39] S. Polatkan and E. Uykur, Optical response of chiral multifold semimetal PdGa, Crystals **11**, 80 (2021).
[40] A. Jain, S. P. Ong, G. Hautier, W. Chen, W. D. Richards, S. Dacek, S. Cholia, D. Gunter, D. Skinner, G. Ceder, and K. a. Persson, The Materials Project: A materials genome approach to accelerating materials innovation, APL Materials **1**, 011002 (2013).
[41] L. Schnatmann, K. Geishendorf, M. Lammel, C. Damm, S. Novikov, A. Thomas, A. Burkov, H. Reith, K. Nielsch, and G. Schierning, Signatures of a charge density wave phase and the chiral anomaly in the fermionic material cobalt monosilicide CoSi, Advanced Electronic Materials **6**, 1900857 (2020).
[42] G. Li, H. Yang, P. Jiang, C. Wang, Q. Cheng, S. Tian, G. Han, C. Shen, X. Lin, H. Lei, W. Ji, Z. Wang, and H.-J. Gao, Chirality locking charge density waves in a chiral crystal, Nature Communications **13**, 2914 (2022).
[43] Z. Rao, Q. Hu, S. Tian, Q. Qu, C. Chen, S. Gao, Z. Yuan, C. Tang, W. Fan, J. Huang, Y. Huang, L. Wang, L. Zhang, F. Li, K. Wang, H. Yang, H. Weng, T. Qian, J. Xu, K. Jiang, H. Lei, Y.-J. Sun, and H. Ding, Charge instability of topological Fermi arcs in chiral crystal CoSi, Science Bulletin **68**, 165 (2023).
[44] W. E. Deeg, S. Subedi, M. Rai, A. Crosbie, M. Zdilla, C. Shekhar, C. Felser, and D. H. Torchinsky, Dataset for: "Enantiomer-Dependent Study of Photogalvanic Effects in the Multifold Fermion PdGa" (2025), tUScholarShare. https://doi.org/10.34944/7dxb-w397.